


 Cite this: *Nanoscale*, 2021, **13**, 8275

## High speed growth of MAPbBr<sub>3</sub> single crystals *via* low-temperature inverting solubility: enhancement of mobility and trap density for photo-detector applications†

 Yunae Cho,<sup>a</sup> Hye Ri Jung,<sup>a</sup> Yeon Soo Kim,<sup>a</sup> Yejin Kim,<sup>a</sup> Joohee Park,<sup>a</sup> Seokhyun Yoon,<sup>a</sup> Yousil Lee,<sup>b</sup> Miyeon Cheon,<sup>b</sup> Se-young Jeong<sup>c</sup> and William Jo<sup>\*,a</sup>

There has been growing interest in organic–inorganic hybrid perovskites as a promising candidate for optoelectronic applications due to their superior physical properties. Despite this, most of the reported perovskite devices based on polycrystalline thin films suffer immensely from poor stability and high trap density owing to grain boundaries limiting their performance. Perovskite single crystal structures have been recently explored to construct stable devices and reduce the trap density compared to their thin-film counterparts. We present a novel method of growing sizable CH<sub>3</sub>NH<sub>3</sub>PbBr<sub>3</sub> single crystals based on the high solubility characteristic of hybrid perovskites at low temperatures within inverse temperature crystallization. We compared both the crystallinity of perovskite single crystal structures and optoelectronic charge transport of single crystal photodetectors as a function of dissolution temperature. The performance of the photodetector fabricated with our large-scaled single crystal with high quality demonstrated low trap density, high mobility, and high photoresponse.

 Received 12th March 2021,  
 Accepted 6th April 2021

DOI: 10.1039/d1nr01600h

[rsc.li/nanoscale](http://rsc.li/nanoscale)

### Introduction

Hybrid metal halide perovskites MAPbX<sub>3</sub> (MA = CH<sub>3</sub>NH<sub>3</sub><sup>+</sup>, X = Cl<sup>−</sup>, Br<sup>−</sup>, or I<sup>−</sup>) have demonstrated high performance owing to their high absorption coefficient, direct bandgap, long carrier lifetime, high mobility, low cost, and facile deposition techniques,<sup>1–7</sup> in optoelectronic applications for solar cells,<sup>1–3</sup> light-emitting diodes,<sup>4,5</sup> photodetectors<sup>6,7</sup> and so on in the past few years. In addition to achieving the high performances of solar cells in a short period,<sup>1</sup> the development of photodetectors has been driven by the beneficial optical and charge-transport properties of perovskites such as high photocurrent, responsivity, and response time.<sup>6</sup> Rapid and great advances of perovskite polycrystalline film photodetectors have been achieved based on the development of the growth technique focusing on large-scale,<sup>6</sup> low-cost solution-process and flexible applications.<sup>7</sup> Beyond polycrystalline perovskite film photodetectors, there have recently been numerous structured per-

ovskite devices such as single crystals<sup>8,9</sup> or low dimensional structures.<sup>10,11</sup> In particular, perovskite single crystals have recently shown superior properties such as longer carrier diffusion lengths, lower trap-state densities and better stability compared to their polycrystalline thin-film counterparts.<sup>8,9,12–23</sup> However, reported perovskite single crystallization processes have some issues of extremely slow growth for large scale or unsatisfactory quality for demanding optoelectronic applications.<sup>15,21–24</sup> Both fast growth and high quality large-scale perovskite single crystals enable a widespread utilization.

Numerous crystallization methods for perovskite single crystals have been introduced such as the conventional cooling technique, antisolvent vapor-assisted crystallization (AVC),<sup>13</sup> top-seeded growth,<sup>14</sup> liquid-diffused separation-induced crystallization,<sup>21</sup> and inverse temperature crystallization (ITC).<sup>15,22,24–26</sup> Bakr *et al.* reported the ITC method to grow high-quality large-scale perovskite single crystals fast, which is a widely used single crystal growth method. Crystallization is induced by reverse solubility dependent on the temperature of hybrid halide perovskites in specific solvents. Unlike the normal dissolution process, most perovskite molecules are bound in the complexes with the solvent, indicating dissolution. In addition, unbound molecules do not reach low-temperature saturation. The increase in temperature decreases

<sup>a</sup>Department of Physics, Ewha Womans University, Korea. E-mail: [wjjo@ewha.ac.kr](mailto:wjjo@ewha.ac.kr)
<sup>b</sup>Crystal Bank Research Institute, Pusan National University, Korea

<sup>c</sup>Department of Optics and Mechatronics Engineering, Pusan National University, Korea

†Electronic supplementary information (ESI) available. See DOI: 10.1039/d1nr01600h

the binding energy of the complexes. Therefore, unbound perovskite molecules increase and nucleation occurs when the solution supersaturates, followed by crystal growth.<sup>15,25</sup> Although the precursor solution for the MAPbBr<sub>3</sub> single crystal was prepared at room temperature,<sup>15,24</sup> there seems to be room for the improvement of this technique considering the reverse solubility of MAPbBr<sub>3</sub> for further high quality and large scale of single crystals.

In this study, an advanced ITC method is proposed by controlling the dissolution temperature. For the first time, the low-temperature inverting solubility of MAPbBr<sub>3</sub> single crystals is demonstrated. We examined the effects of dissolution temperature on the MAPbBr<sub>3</sub> quality and a single crystal device as a representative hybrid halide perovskite material. High quality and large-scale MAPbBr<sub>3</sub> single crystals were fabricated with fast processing based on complete dissolution at low temperatures and fine heating control. The structural, optical, and electrical properties of single crystals grown at three dissolving temperatures were compared to investigate the essential parameters affecting the device performance. Furthermore, we demonstrated the potential to utilize a perovskite single crystal in practical optoelectrical application for observing the charge transport properties. The low temperature crystallization technique can be applied to numerous perovskite single crystal growth, which contributes to their high quality and large scale for the wide perovskite-based applications.

## Results

In the solution-based perovskite single crystal growth, complete dissolution without residual molecules and growth temp-

erature control are important factors in determining the quality of single crystals. Fig. 1 shows the low temperature inverting solubility with the dissolution mechanism depending on different temperatures, fine heating rate control and then the resulting CH<sub>3</sub>NH<sub>3</sub>PbBr<sub>3</sub> (MAPbBr<sub>3</sub>) single crystals. The inverse temperature crystallization (ITC) method showed that the elevation of temperature leads to the crystallization of the precursor solution dissolved at low temperatures.<sup>15,25</sup> This is related to the paradoxical solubility of the hybrid perovskite compound as opposed to a common monomolecular compound at high temperature.<sup>15,25,26</sup> In Fig. 1a, as the advanced ITC technique, we devise the low temperature dissolution below 0 °C based on the measurement of low temperature inverting solubility for the first time, and the method of implementing them in detail is presented in Fig. S1.† According to the solubility and freezing temperature of the *N,N*-dimethylmethanamide (DMF) solvent (−61 °C), we dissolved a precursor solution at the low temperature (LT) of −40 °C, which was determined from the respective solubility of MAPbBr<sub>3</sub>. It consisted of the MAPbBr<sub>3</sub>-DMF complex under the more completely and clearly dissolved condition compared to the zero temperature (ZT) at 0 °C, and room temperature (RT) at 20 °C using undissolved precursors, as shown in Fig. 1a. Three different dissolution temperatures—RT, ZT, and LT—were kept in each bath using air, ice, and dry ice to compare the crystallization. Fig. 1b illustrates the heating rate of the crystallization in three different regions and the growing process at each temperature. In the ITC method, controlling the heating temperature was introduced to maintain constant temperature<sup>15</sup> or extremely slow increase.<sup>24</sup> Although crystallization with high quality is required over the longest possible time period theoretically, the reasonable adjustment of the process time should

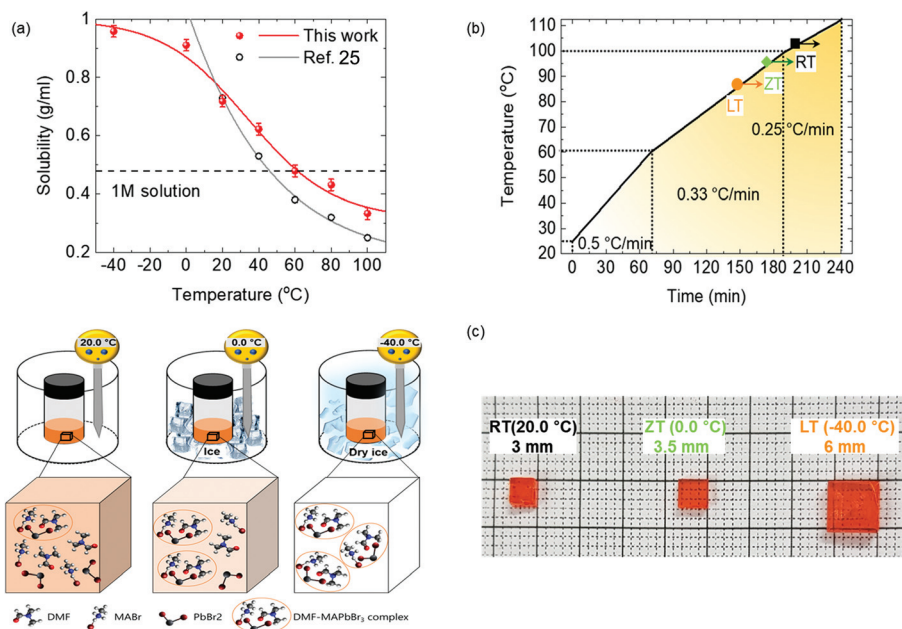


**Fig. 1** (a) Temperature-dependent solubility of MAPbBr<sub>3</sub> in DMF compared to ref. 21 and schematic diagram of dissolution temperature control, (b) heating rate of crystallization for high speed process, (c) MAPbBr<sub>3</sub> single crystal size at different dissolution temperatures.

be necessary for commercial applications. Therefore, our gradient heating rate technique provides both the high quality and large size of single crystals for efficient time utilization within 6 h only. The heating rate was  $0.5\text{ }^{\circ}\text{C min}^{-1}$  between  $20\text{ }^{\circ}\text{C}$  and  $60\text{ }^{\circ}\text{C}$ , while it decreased gradually to  $0.33\text{ }^{\circ}\text{C min}^{-1}$  between  $60\text{ }^{\circ}\text{C}$  and  $100\text{ }^{\circ}\text{C}$ ; furthermore, it decreased to  $0.25\text{ }^{\circ}\text{C min}^{-1}$  over  $100\text{ }^{\circ}\text{C}$ . Particularly, the period from  $20\text{ }^{\circ}\text{C}$  to  $60\text{ }^{\circ}\text{C}$  is the preparatory zone, where seed crystals are formed. The adaptation of the highest heating rate ( $0.5\text{ }^{\circ}\text{C min}^{-1}$ ) on this zone leads to a significantly shorter time for the whole crystallization process compared to the results presented in previous literature.<sup>24</sup> It demonstrated rapid crystal growth in low temperature period does not affect the realization of high quality according to our results of crystallization. Rather, the increase in the crystal size is prominently due to the increase in temperature in the high temperature period, as shown in Fig. S2,<sup>†</sup> which it can be seen synthetically that slow growth rate in high temperature region further helps to form the large crystal than controlling heating rate in low temperature region. In addition, although the heating temperature was controlled from  $20\text{ }^{\circ}\text{C}$  to  $110\text{ }^{\circ}\text{C}$  to the three different dissolution conditions equally, the temperature at which the seed crystal forms was different, corresponding to the point and arrow in Fig. 1b; at the lower dissolution temperature, the seed of single crystal was formed at a lower temperature as the starting point of the growth of single crystals. This also seems to potentially affect the final formation. Fig. 1c shows the largest MAPbBr<sub>3</sub> single crystal at the lowest dissolution temperature with a parallelepiped shape. The size distribution of the crystal growth as the dissolution temperature was investigated *via* the repeated crystallization process, as shown in Fig. S3.<sup>†</sup> The relationship between the number of single crystals and crystal sizes shows that large-sized single crystals were distributed with the decrease in the dissolution temperature. In addition, the surface and cross-section images of single crystals *via* scanning electron microscopy (SEM) are shown in Fig. S4.<sup>†</sup> The image of single crystals in the LT condition was obtained only due to more deterioration of single crystals with ZT and RT conditions than that with the LT condition, which suggests the relationship between the quality and bonding of single crystals.

The X-ray diffraction (XRD) analysis of MAPbBr<sub>3</sub> single crystals confirmed the crystalline quality, as shown in Fig. 2. Fig. 2a shows very sharp peaks in the XRD of powder single crystal, corresponding to the (001), (110), (002), (210), (211), (220), and (003) planes of the cubic MAPbBr<sub>3</sub> crystal structure.<sup>24,27</sup> Moreover, the maximal facet of MAPbBr<sub>3</sub> single crystal XRD shows only (001), (002), and (003) peaks, indicating the superiority of a well-structured single crystal out of all single crystals with different dissolved temperatures.<sup>17,24</sup> Furthermore, the first major XRD peaks were examined by high-resolution X-ray rocking curve analyses using full width at half maximum (FWHM) to compare the fine crystalline quality of three single crystals with different dissolved temperatures (see Fig. 2b). Single crystals in RT, ZT, and LT conditions showed  $0.0253^{\circ}$ ,  $0.0179^{\circ}$ , and  $0.0171^{\circ}$  FWHM, respectively; it suggests that the quality of single crystals in the LT condition is the best than those with other dissolved temperatures. FWHM of our single crystal demonstrates the superior quality of crystallization in the LT condition than the other reference values of MAPbBr<sub>3</sub> single crystals in the literatures.<sup>17,24,27</sup> In addition, the single crystal X-ray diffraction of our MAPbBr<sub>3</sub> single crystal confirmed that it had a cubic crystal structure and space group no. 221 (*Pm3m*) with the lattice constant  $a = 5.907\text{ \AA}$ , as shown in the inset of Fig. 2b, which is similar to the literature.<sup>15</sup>

The optical and optoelectronic properties of three different single crystals were investigated, as shown in Fig. 3. Raman spectra of every single crystal confirmed MAPbBr<sub>3</sub> crystal phases with a cubic structure.<sup>28,29</sup> The vibration modes associated with organic atoms were observed above  $200\text{ cm}^{-1}$ , as listed in Table 1. The observed modes from three different samples were similar to those from the references and thus assigned accordingly.<sup>30,31</sup> Specifically, the peak intensity of the  $\nu_1$  (C–N torsion) mode was higher and the linewidth was narrower for a single crystal grown in the LT condition, which demonstrates that this crystal exhibits better crystalline quality than other crystals under RT and ZT conditions.<sup>32</sup> The photoluminescence (PL) spectra exhibit one sharp peak at  $2.29\text{ eV}$  ( $541\text{ nm}$  wavelength) for all the samples as is known in the literature.<sup>15</sup> However, the difference of the PL peak at several measuring points of the sample is the smallest in the crystal

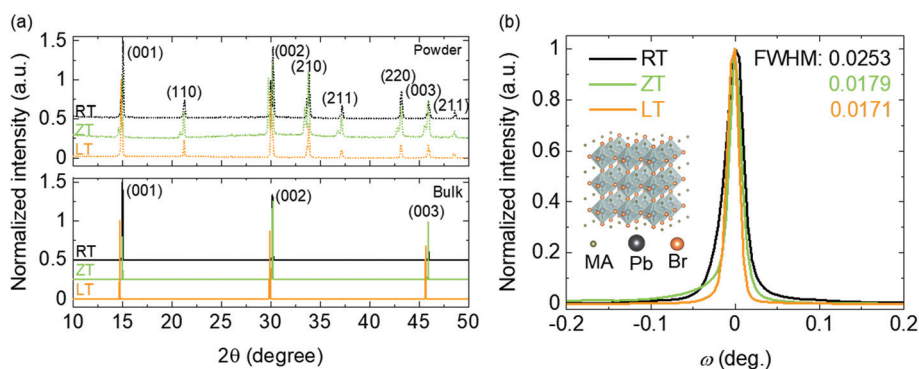


Fig. 2 X-ray diffraction of (a) powder and single crystal. (b) Rocking curve with different dissolution temperature.

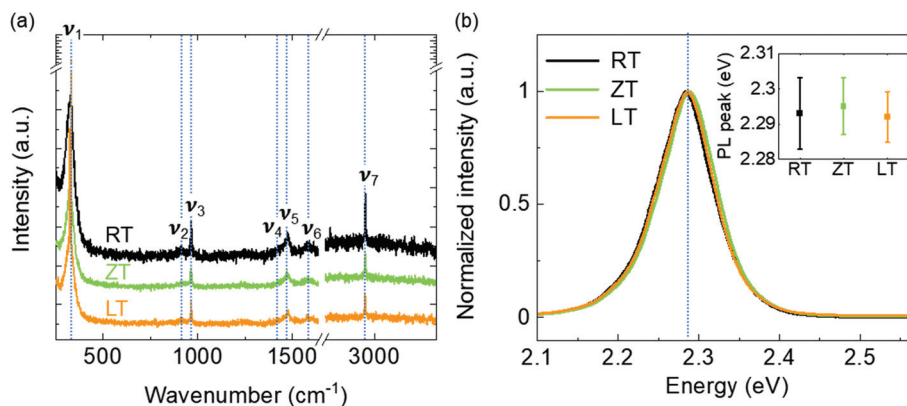


Fig. 3 (a) Raman and (b) PL spectra of MAPbBr<sub>3</sub> single crystal with different dissolved temperatures.

Table 1 Raman shift of MAPbBr<sub>3</sub> single crystals from the literature<sup>24,27</sup>

Peaks (RT)	Position (cm <sup>-1</sup> )	Vibrational modes assignments (80 K)
ν <sub>1</sub>	327	C-N torsion τ (MA)
ν <sub>2</sub>	916	MA rocking ρ (MA)
ν <sub>3</sub>	970	C-N stretching ν (C-N)
ν <sub>4</sub>	1457	CH <sub>3</sub> asymmetric bending δ <sub>as</sub> (CH <sub>3</sub> )
ν <sub>5</sub>	1471	NH <sub>3</sub> symmetric bending δ <sub>s</sub> (NH <sub>3</sub> )
ν <sub>6</sub>	1589	NH <sub>3</sub> asymmetric bending δ <sub>as</sub> (NH <sub>3</sub> )
ν <sub>7</sub>	2957	CH <sub>3</sub> asymmetric stretching ν <sub>as</sub> (CH <sub>3</sub> )

in the LT condition, suggesting that uniformity of the LT sample is slightly better than other samples, as shown in the inset of Fig. 3b. In addition, the absorption of single crystal in the LT condition was investigated to be better than that of others, as shown in Fig. S5.†

The carrier transport in dark was characterized by the space-charge-limited current (SCLC) method,<sup>33</sup> as shown in Fig. 4. Although the mobility and carrier concentration of the semiconductor are accurately observed by the Hall effect

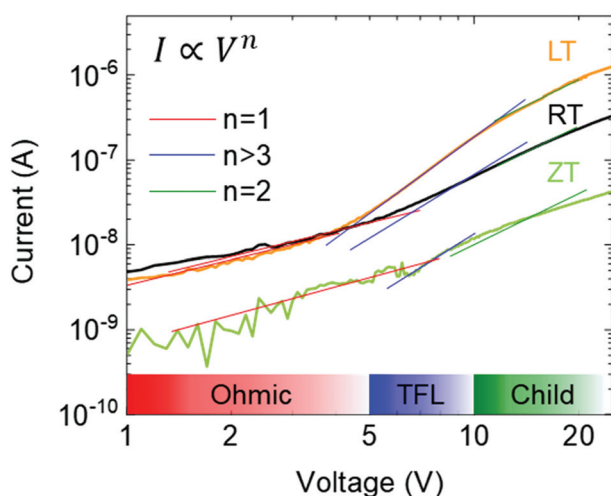


Fig. 4 Dark *I*-*V* characteristics using SCLC method.

measurement, the SCLC method was carried because the conductivity of our single crystals is within the measurement limit<sup>34,35</sup>. In particular, it shows the dark *I*-*V* properties of single crystals with different dissolved temperatures. The *I*-*V* curves are divided into three regions: ohmic (red line), trap-filling region (blue line), and trap free (green line). The trap density ( $n_{\text{trap}}$ ) can then be determined by the trap-filled limit voltage,  $V_{\text{TFL}}$ , the voltage at which the current begins to increase rapidly using following the equation:<sup>33,36</sup>

$$n_t = \frac{2V_{\text{TFL}}\epsilon_r\epsilon_0}{eL^2}, \quad (1)$$

where  $\epsilon_0$  is the vacuum permittivity,  $\epsilon_r$  is the relative dielectric constant ( $\epsilon_r = 25.5$ ),<sup>37</sup>  $e$  is the elementary charge ( $1.6 \times 10^{-19}$  C), and  $L$  is the single-crystal thickness. The trap densities of a single crystal with different dissolved temperatures were determined according to the equation (see Table 2). It was found by comparing the trap densities that the performance of the single crystal device was the best in the LT condition. Moreover, within the reported trap density range of  $26\text{--}200 \times 10^9 \text{ cm}^{-3}$  for the MAPbBr<sub>3</sub> single crystals,<sup>19</sup> the ones produced in the LT condition are better than those produced under other dissolution temperature conditions. The carrier mobility over approximately 10 V of the single crystal was extracted by fitting the Mott-Gurney law:<sup>15,38</sup>

$$J_d = \frac{9\epsilon_r\epsilon_0\mu V^2}{8L^3}, \quad (2)$$

where  $J_d$  is the dark current density,  $\mu$  is the mobility, and  $V$  is the voltage. The mobility of the single crystal device in the LT

Table 2 Comparison of carrier transport

Temperature	Conductivity ( $\Omega^{-1} \text{ cm}^{-1}$ )	Trap density ( $\text{cm}^{-3}$ )	Mobility ( $\text{cm}^2 \text{ V}^{-1} \text{ s}^{-1}$ )	Hole concentration ( $\text{cm}^{-3}$ )
RT	$2.18 \times 10^{-8}$	$6.59 \times 10^9$	18	$2.55 \times 10^{12}$
ZT	$3.31 \times 10^{-9}$	$3.06 \times 10^9$	6	$1.42 \times 10^{11}$
LT	$1.53 \times 10^{-8}$	$2.55 \times 10^9$	115	$1.10 \times 10^{13}$

condition was  $115 \text{ cm}^2 \text{ V}^{-1} \text{ s}^{-1}$ , which is extremely larger than its microcrystalline thin-film counterpart<sup>6</sup> and the single crystals grown using ITC.<sup>15,20</sup> Moreover, the conductivity,  $\sigma$ , of the ohmic region and hole concentration,  $n_c$ , are calculated using the following equation:<sup>20</sup>

$$n_c = \frac{\sigma}{e\mu} \quad (3)$$

The values derived by fitting eqn (3) are listed in Table 2. The values indicate that the single crystal in the LT condition is superior in quality for photosensor applications than those MAPbBr<sub>3</sub> single crystals grown using other techniques.<sup>15,20</sup> The statistical results of these electrical measurements have supported the reliability of our technique for high-quality single crystal photodetectors (Fig. 5). The performance of photodetectors, such as photocurrent, responsivity and

response time in single crystals, was investigated under white light with  $5 \text{ mW cm}^{-2}$ . The  $I$ - $V$  curves of the single-crystal device were measured, as shown in Fig. 6a. The photo current density was approximately  $10^{-3} \text{ A cm}^{-2}$ , as expected from the high-quality single crystal.<sup>20</sup> The high-quality photodetector fabricated in the LT condition shows the largest photo current density. Fig. 6b shows the time-dependent photoresponse of the single crystal device under white light and 2 V bias. In addition, the calculated responsivities,  $R$  of LT, ZT, RT samples are 0.059, 0.052, and  $0.058 \text{ A W}^{-1}$ , respectively, using the following equation:

$$R = \frac{J_{\text{ph}} - J_{\text{d}}}{P_{\text{in}}}$$

where  $J_{\text{ph}}$  is the photocurrent density and  $P_{\text{in}}$  is the incident light power density.

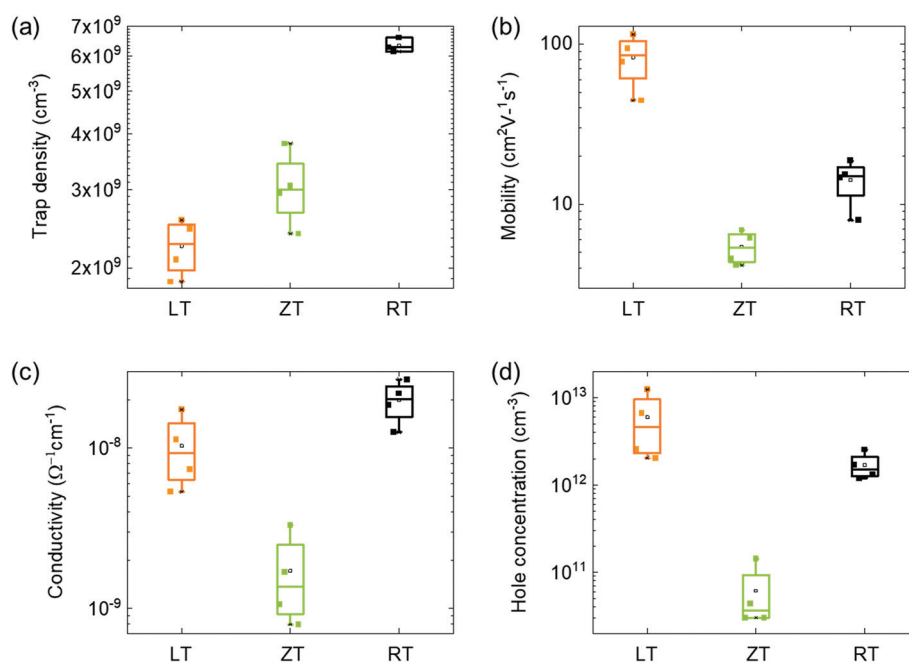


Fig. 5 (a) Trap density, (b) mobility, (c) conductivity, (d) hole concentration of MAPbBr<sub>3</sub> single crystals with different dissolution condition.

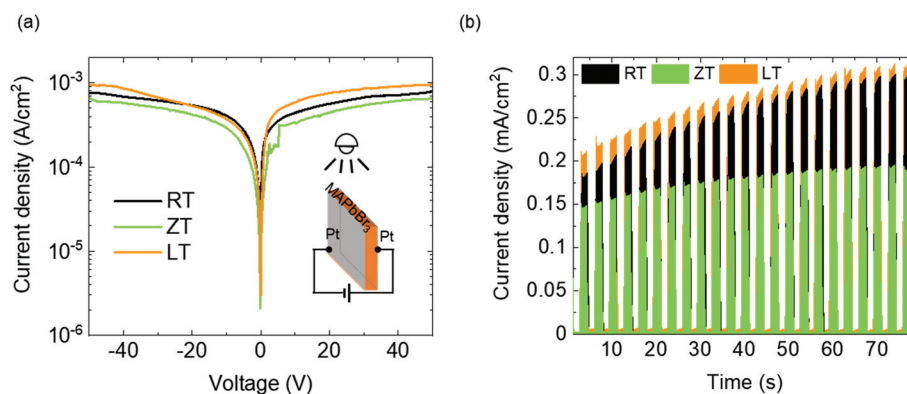


Fig. 6 (a) Photocurrent–voltage ( $I$ - $V$ ) curves of the photodetector and (b) on–off photoresponse at 2 V bias voltage under the white light.

The responsivity of LT samples was slightly higher than that of others. In the measurement of response time shown in Fig. 7, a rapid increase in time (<20 ns) (the inset of Fig. 7) and slow decay time of single crystals can be observed. The decay times of LT, ZT, RT samples are 500, 470, 430  $\mu\text{s}$ , respectively.

Numerous cycles of photocurrent density of this device indicate the reproducibility and stability of our single crystal photodetectors without any degradation. Table 3 shows the photoresponse characteristics of the reported MAPbBr<sub>3</sub> single crystal photodetector, including the result of this work. Despite the active research on MAPbBr<sub>3</sub> single crystals, its previous researches on photocurrent are rare and their performances are not high.<sup>20–23</sup> Fig. 6b surprisingly shows that not only did the LT state single crystal device exhibit the highest photocurrent density under all conditions, our results are the best among the previous literatures. Indeed, the increasing photocurrent depending on the illumination time is observed in Fig. 6b. One of causes for this behavior was suggested as the light trapping mediated by defect states, such as other optoelectronic devices.<sup>39</sup> According to the recent research, the increasing photocurrent can be caused by the change of mobility.<sup>40</sup> However, the mechanism study requires a detailed investigation of the carrier transport for perovskite materials, which is a subject of future research.

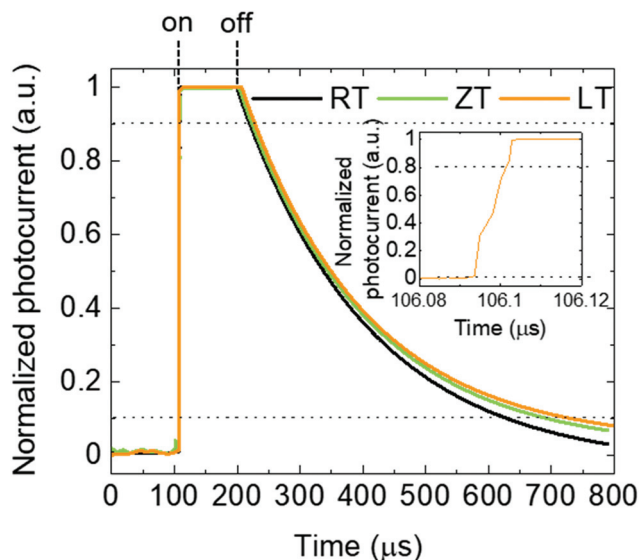


Fig. 7 Response times of MAPbBr<sub>3</sub> single crystals with different dissolution conditions.

Table 3 Summary of the reported MAPbBr<sub>3</sub> single crystal photodetectors

Fabrication method	Bias voltage (V)	Light source	Light intensity ( $\text{mW cm}^{-2}$ )	Photocurrent density ( $\mu\text{A cm}^{-2}$ )	Ref.
ITC	2	White light	5	314	This work
LDSC	-4	White light	—	200	17
ITC	4	525 nm	60	100	16
ITC	1.5	405 nm	—	25	18
Mixed halide crystallization	-4	White light	0.4	0.04	19

## Conclusion

We fabricated high quality MAPbBr<sub>3</sub> single crystals and related optoelectronic devices with a low dissolution temperature (LT) based on the ITC method. Moreover, the low temperature inverting solubility was demonstrated in this study for the first time. The gradient heating rate led to a reduction in the growth processing time and high-quality large-scale single crystals. Improved crystalline quality in the LT condition, out of the three dissolved temperatures, was demonstrated owing to the narrow XRD rocking curve, high-intensity Raman peak, and spatial uniformity of PL peak. We show the potential of applying MAPbBr<sub>3</sub> single crystals to the photodetector using a carrier transport in dark and illumination conditions. The SCLC analysis exhibited surprisingly low trap density and high mobility of single crystal devices formed in the LT condition. The photoresponse of the device was superior to the other two dissolution conditions as well as better than the reported results. This technology has great potential due to its scalability to various perovskite materials with inverse solubility and the simple and clear industrial application. Our novel growth technique with excellent optoelectronic properties of MAPbBr<sub>3</sub> single crystals can contribute to manufacturing high-quality perovskite single crystals for the next generation optoelectronic devices.

## Experimental method

### Synthesis of MAPbBr<sub>3</sub> single crystals

Methylammonium lead bromide (MAPbBr<sub>3</sub>) single crystals were grown based on the ITC method.<sup>15</sup> Methylammonium bromide and lead bromide (PbBr<sub>2</sub>) were mixed with 1:1 (PbBr<sub>2</sub>:MABr) in *N,N*-dimethylformamide (DMF) to prepare the growth solution. The temperature was set at three different values using ice and dry ice bath to dissolve the precursors. The solution was sonicated for 10 min for further dissolution and homogenization. Thereafter, it was filtered using a 0.2  $\mu\text{m}$  PTFE filter. After filtration, the solution was divided among vials in 2 mL quantities and placed on the hotplate on a computational heating system. After growth, the crystals were dried in a vacuum chamber, as shown in Fig. S1.†

### Solubility test

2 ml of DMF in a vial was placed on a hot plate under stirring. Keeping the temperature, we started dissolving the amount of MABr and PbBr<sub>2</sub> powder expected to be completely dissolved

at the temperature in DMF. After checking the transparent solution, we added small amount of powder equivalent to 0.1 M. The same process was repeated at different temperatures. Temperatures of 0 and  $-40$  °C have been investigated in the same method, but keeping the vial in an ice and dry ice bath.

### Fabrication of the photodetector device

A photodetector was fabricated by depositing  $\approx 100$  nm Pt electrodes *via* vacuum sputtering on the single-crystalline perovskite MAPbBr<sub>3</sub>, which is the sandwich structure. On average, the sizes of the single crystal device in LT, ZT, RT condition are about 4 mm  $\times$  4 mm  $\times$  2 mm.

### X-ray diffraction

X-ray diffraction (XRD) patterns of the MAPbBr<sub>3</sub> powder and bulk of single crystal were recorded on an X-ray diffractometer (PANalytical, X'Pert Pro MPD) using a Cu-K $\alpha$  ( $\lambda = 1.5418$  Å) radiation source (40 kV, 30 mA).

### Single crystal X-ray diffraction

The crystal structures of MAPbBr<sub>3</sub> were ascertained by standard crystallographic methods. Orange block-shaped crystals were used for single-crystal X-ray diffraction. The data were collected at 223(2) K using a Bruker D8 Venture equipped with a  $\mu$ S micro-focus sealed tube Mo K $\alpha$  ( $\lambda = 0.71073$  Å) and a PHOTON III M14 detector in Western Seoul Center of Korea Basic Science Institute. Data collection and integration were performed using the SMART APEX3 software package (SAINT+). Moreover, absorption correction was performed by the multi-scan method implemented in SADABS. The structure was solved by direct methods and refined by full-matrix least-squares on  $F^2$  using the SHELXTL program package (version 6.14).

### Raman spectroscopy and photoluminescence

Raman scattering spectroscopy was performed to identify the phase formation of the material. All spectra were recorded using a McPherson 207 spectrometer equipped with a TE-cooled charge-coupled-device (CCD) array detector at room temperature. The samples were excited with 7.25 mW of a 632.8 nm He-Ne laser, focused to a  $\sim 1$  mm diameter spot using a microscope objective (100 $\times$ ). Room temperature photoluminescence (PL) spectra were recorded to characterize bandgap energies. We used 0.5 mW of a 488 nm diode laser as an excitation source.

### Space charge limited current (SCLC) and photoresponse measurement

A photodetector was fabricated by depositing  $\approx 100$  nm Pt electrodes on both the sides of the perovskite MAPbBr<sub>3</sub> single crystal *via* vacuum sputtering. The SCLC measurement was performed using a Keithley 2400 source-meter in dark at room temperature. The current-voltage ( $I$ - $V$ ) measurements were performed on a probe station connected to a Keithley 4200 semiconducting analyzer. The photoresponse was measured using white light having the intensity of 5 mW cm<sup>-2</sup>. The

single normalized on/off cycle of the photocurrent was at a frequency of 30 Hz. The response time was measured by an Agilent Technologies DSO6054A oscilloscope with a 2 M $\Omega$  resistor.

## Author contributions

Yunae Cho: Conceptualization, data curation, investigation, methodology, writing – original draft. Hye Ri Jung: Conceptualization, methodology. Yeon Soo Kim: Investigation. Yejin Kim: Investigation. Joohee Park: Investigation. Seokhyun Yoon: Validation, writing – review & editing. Yousil Lee: Methodology. Miyeon Cheon: Methodology, validation. Se-young Jeong: Methodology, validation. William Jo: Supervision, validation, writing – review and editing.

## Conflicts of interest

There are no conflicts of interest to declare.

## Acknowledgements

This research was supported by Basic Science Research Program through the National Research Foundation of Korea (NRF) funded by the Ministry of Education (NRF-2018R1A6A1A03025340, NRF-2016R1D1A1B01009032, and NRF-2020R1I1A1A01068700) and by the Ministry of Science, ICT & Future Planning (NRF-2017R1A2B3011822).

## References

- 1 N.-G. Park, *Adv. Energy Mater.*, 2020, **10**, 1903106.
- 2 S. Liu, Y. Guan, Y. Sheng, Y. Hu, Y. Rong, A. Mei and H. Han, *Adv. Energy Mater.*, 2020, **10**, 1902492.
- 3 M. Jung, S.-G. Ji, G. Kim and S. I. Seok, *Chem. Soc. Rev.*, 2019, **48**, 2011–2038.
- 4 M. Lu, Y. Zhang, S. Wang, J. Guo, W. W. Yu and A. L. Rogach, *Adv. Funct. Mater.*, 2019, **29**, 1902008.
- 5 S. D. Stranks, R. L. Z. Hoyer, D. Di, R. H. Friend and F. Deschler, *Adv. Mater.*, 2019, **31**, 1803336.
- 6 J. Miao and F. Zhang, *J. Mater. Chem. C*, 2019, **7**, 1741–1791.
- 7 D. Hao, J. Zou and J. Huang, *InfoMat*, 2020, **2**, 139–169.
- 8 Q. Dai, X. Chen, R. Ding, Y. Peng, W. Lv, Z. Zhou, S. Xu and L. Sun, *Opt. Mater.*, 2021, **111**, 110684.
- 9 K. Wang, L. Jing, Q. Yao, J. Zhang, X. Cheng, Y. Yuan, C. Shang, J. Ding, T. Zhou, H. Sun, W. Zhang and H. Li, *J. Phys. Chem. Lett.*, 2021, **12**, 1904–1910.
- 10 S. Wang, Y. Chen, J. Yao, G. Zhao, L. Li and G. Zou, *J. Mater. Chem. C*, 2021, DOI: 10.1039/D1TC00408E.
- 11 H.-P. Wang, S. Li, X. Liu, Z. Shi, X. Fang and J.-H. He, *Adv. Mater.*, 2021, **33**, 2003309.

- 12 X. D. Wang, W. G. Li, J. F. Liao and D. B. Kuang, *Sol. RRL*, 2019, **3**, 1800294.
- 13 D. Shi, V. Adinolfi, R. Comin, M. Yuan, E. Alarousu, A. Buin, Y. Chen, S. Hoogland, A. Rothenberger, K. Katsiev, Y. Losovyj, X. Zhang, P. A. Dowben, O. F. Mohammed, E. H. Sargent and O. M. Bakr, *Science*, 2015, **347**, 519–522.
- 14 Q. Dong, Y. Fang, Y. Shao, P. Mulligan, J. Qiu, L. Cao and J. Huang, *Science*, 2015, **347**, 967–970.
- 15 M. I. Saidaminov, A. L. Abdelhady, B. Murali, E. Alarousu, V. M. Burlakov, W. Peng, I. Dursun, L. Wang, Y. He, G. Maculan, A. Goriely, T. Wu, O. F. Mohammed and O. M. Bakr, *Nat. Commun.*, 2015, **6**, 7586.
- 16 X. Jiang, X. Fu, D. Ju, S. Yang, Z. Chen and X. Tao, *ACS Energy Lett.*, 2020, **5**, 1797–1803.
- 17 W. Peng, L. Wang, B. Murali, K.-T. Ho, A. Bera, N. Cho, C.-F. Kang, V. M. Burlakov, J. Pan, L. Sinatra, C. Ma, W. Xu, D. Shi, E. Alarousu, A. Goriely, J.-H. He, O. F. Mohammed, T. Wu and O. M. Bakr, *Adv. Mater.*, 2016, **28**, 3383–3390.
- 18 J. Huang, Y. Shao and Q. Dong, *J. Phys. Chem. Lett.*, 2015, **6**, 3218–3227.
- 19 H.-S. Rao, W.-G. Li, B.-X. Chen, D.-B. Kuang and C.-Y. Su, *Adv. Mater.*, 2017, **29**, 1602639.
- 20 Y. Liu, Y. Zhang, K. Zhao, Z. Yang, J. Feng, X. Zhang, K. Wang, L. Meng, H. Ye, M. Liu and S. Liu, *Adv. Mater.*, 2018, **30**, 1707314.
- 21 F. Yao, J. Peng, R. Li, W. Li, P. Gui, B. Li, C. Liu, C. Tao, Q. Lin and G. Fang, *Nat. Commun.*, 2020, **11**, 1194.
- 22 H.-H. Fang, S. Adjokatse, H. Wei, J. Yang, G. R. Blake, J. Huang, J. Even and M. A. Loi, *Sci. Adv.*, 2016, **2**, e1600534.
- 23 Y. Fang, Q. Dong, Y. Shao, Y. Yuan and J. Huang, *Nat. Photonics*, 2015, **9**, 679–686.
- 24 Y. Liu, Y. Zhang, Z. Yang, J. Feng, Z. Xu, Q. Li, M. Hu, H. Ye, X. Zhang, M. Liu, K. Zhao and S. Liu, *Mater. Today*, 2019, **22**, 67–75.
- 25 M. I. Saidaminov, A. L. Abdelhady, G. Maculan and O. M. Bakr, *Chem. Commun.*, 2015, **51**, 17658–17661.
- 26 G. Maculan, A. D. Sheikh, A. L. Abdelhady, M. I. Saidaminov, M. A. Haque, B. Murali, E. Alarousu, O. F. Mohammed, T. Wu and O. M. Bakr, *J. Phys. Chem. Lett.*, 2015, **6**, 3781–3786.
- 27 J. T. Tisdale, T. Smith, J. R. Salasin, M. Ahmadi, N. Johnson, A. V. Ievlev, M. Koehler, C. J. Rawn, E. Lukosi and B. Hu, *CrystEngComm*, 2018, **20**, 7818–7825.
- 28 L. C. Schmidt, A. Pertegás, S. González-Carrero, O. Malinkiewicz, S. Agouram, G. M. Espallargas, H. J. Bolink, R. E. Galian and J. Pérez-Prieto, *J. Am. Chem. Soc.*, 2014, **136**, 850–853.
- 29 H. R. Jung, G. Y. Kim, B. P. Nguyen, H.-J. Jin, W. Jo, T. T. T. Nguyen, S. Yoon, W. S. Woo, C. W. Ahn, S. Cho and I. W. Kim, *J. Phys. Chem. Lett.*, 2017, **121**, 21930–21934.
- 30 L.-Q. Xie, T.-Y. Zhang, L. Chen, N. Guo, Y. Wang, G.-K. Liu, J.-R. Wang, J.-Z. Zhou, J.-W. Yan, Y.-X. Zhao, B.-W. Mao and Z.-Q. Tian, *Phys. Chem. Chem. Phys.*, 2016, **18**, 18112–18118.
- 31 T. Zhang, L. Xie, L. Chen, N. Guo, G. Li, Z. Tian, B. Mao and Y. Zhao, *Adv. Funct. Mater.*, 2017, **27**, 1603568.
- 32 M. R. Joya, K. M. Fonseca and J. Barba-Ortega, *AIP Conf. Proc.*, 2014, **1627**, 42–45.
- 33 R. H. Bube, *J. Appl. Phys.*, 1962, **33**, 1733–1737.
- 34 O. S. Mortensen, R. W. Munn and D. F. Williams, *J. Appl. Phys.*, 1971, **42**, 1192–1203.
- 35 T. Yamasaki, K. Ueno, A. Tsukazaki, T. Fukumura and M. Kawasaki, *Appl. Phys. Lett.*, 2011, **98**, 082116.
- 36 P. Mark and W. Helfrich, *J. Appl. Phys.*, 1962, **33**, 205–215.
- 37 A. Poglitsch and D. Weber, *J. Chem. Phys.*, 1987, **87**, 6373–6378.
- 38 J. Xing, Y. Zou, C. Zhao, Z. Yu, Y. Shan, W. Kong, X. Zheng, X. Li, W. Yu and C. Guo, *Mater. Today Phys.*, 2020, **14**, 100240.
- 39 Y. Cho, J. Hwang, I. Jeong, J. Gwak, J. H. Yun, K. Kim and W. Jo, *Sol. Energy Mater. Sol. Cells*, 2021, **220**, 110860.
- 40 C. L. Watts, L. Aspirtarte, Y.-H. Lin, W. Li, R. Elzein, R. Addou, M. J. Hong, G. S. Herman, H. J. Snaith and J. G. Labram, *Commun. Phys.*, 2020, **3**, 73.